X-ray magneto-optical polarization spectroscopy: an analysis from the visible region to the x-ray regime

M. F. Tesch,[1,*] M. C. Gilbert,[1] H.-Ch. Mertins,[1] D. E. Bürgler,[2] U. Berges,[3] and C. M. Schneider[2,4]

[1]University of Applied Sciences Münster, Stegerwaldstrasse 39, Steinfurt D-48565, Germany

[2]Peter Grünberg Institut (PGI-6) and Jülich-Aachen Research Alliance (JARA-FIT), Forschungszentrum Jülich GmbH, Jülich D-52425, Germany

[3]DELTA, Maria-Goeppert-Mayer-Straße 2, Dortmund D-44227, Germany

[4]Fakultät f. Physik and Center for Nanointegration Duisburg-Essen (CENIDE), Universität Duisburg-Essen, Duisburg D-47048, Germany

*Corresponding author: marc.tesch@fh-muenster.de

Received 22 March 2013; accepted 24 April 2013;
posted 20 May 2013 (Doc. ID 187525); published 18 June 2013

An ultra-high vacuum compatible multipurpose chamber for magneto-optical reflection and transmission experiments with polarization analysis on magnetic systems is introduced. It is applicable in a broad photon energy range from the visible to the soft x-ray regime and for a wide angular range from grazing to normal incidence. It exploits a novel magnetization device based on rotating permanent magnets, which generates tuneable magnetic fields up to 570 mT in longitudinal, transverse and polar geometry. The unique combination of these features enables the feasibility of all typical magneto-optical spectroscopy techniques as T-MOKE, L-MOKE, P-MOKE, x-ray magneto optical linear dichroism, x-ray magnetic circular dichroism in reflection and Kerr polarization-spectroscopy, which is demonstrated for Co with focus on the Co 3*p* edges.

OCIS codes: (160.3820) Magneto-optical materials; (340.7480) X-rays, soft x-rays, extreme ultraviolet (EUV); (340.6720) Synchrotron radiation; (120.2130) Ellipsometry and polarimetry; (000.3110) Instruments, apparatus, and components common to the sciences.

http://dx.doi.org/10.1364/AO.52.004294

1. Introduction

Magneto-optical spectroscopies provide an essential and versatile toolbox for the characterization, investigation and development of magnetic materials and devices [1,2]. Among these the spectroscopies which utilize synchrotron radiation, as e.g., the x-ray magnetic circular dichroism (XMCD) typically detected in absorption, reflection or photoelectron spectroscopy [3–5] or the x-ray magnetic linear dichroism (XMLD) [4,6] are established as leading-edge research techniques for the study of both fundamental and applied aspects of magnetism. These x-ray techniques allow for element-selective investigations of magnetic properties of individual constituents in complex magnetic materials as well as for the element-selective imaging of magnetic domain structures [7–10], which on such detailed level are not possible with visible light. An important development in x-ray magneto-optical spectroscopies is the polarization spectroscopy, which can provide the full polarization state of the light after

1559-128X/13/184294-17$15.00/0

its interaction with the sample. Important representatives are the x-ray Faraday effect [11,12], the x-ray Kerr-effect, which may be observed in the longitudinal (L-MOKE) or polar (P-MOKE) geometry [4,13,14], and the x-ray Voigt effect [15]. In contrast to absorption or intensity measurements the polarization analysis reveals additional information, which enables for example the determination of the complete set of magneto-optical constants. One general advantage of magneto-optical spectroscopies over photoelectron spectroscopy is the compatibility with applied high magnetic fields. A second advantage is the tunability of the information depth over several orders of magnitude by using photons from the visible regime up to the soft x-ray range. Photoelectrons typically emanate from a limited depth near the surface region and thus often require clean surfaces and *in situ* techniques. In contrast the presented so-called photon-in-photon-out spectroscopies allow for scanning the depth profile of chemical and/or magnetic parameters in layered systems or buried structures by tuning the angle of incidence of the incoming light [1]. Thus, these photon-in–photon-out spectroscopies are particularly useful for the characterization of industrial samples with imperfect surfaces.

Depending on the polarization state of light and the geometrical arrangement of the spin quantization axis in the magnetic material magneto-optical spectroscopies allow for the separation of signals from ferromagnetic and even antiferromagnetic (AFM) layers [16]. AFMs are of current interest, because they meet key applications in novel spintronic devices, such as magneto-resistive, spin-valve and exchange biased materials and nanostructures [2,17–19], which often employ buried AFM layers coupled to ferromagnetic layers to define a magnetic reference orientation.

In the visible light range the related magneto-optical techniques are widely exploited standard tools for the examination of the electronic structure of magnetic materials [20] as well as for characterization of magnetism and microscopy of magnetic domains [20]. While these magneto-optical effects are usually small in the visible, much larger effects are observed in the extreme ultraviolet (EUV) and soft x-ray regimes due to the resonant enhancement occurring at the $3p$ and $2p$ edges of $3d$-transition metals [1,3,4,21] and the $3d$ edges of rare-earth elements [22]. Thus, the development of polarization-sensitive techniques in the soft x-ray range may open up new avenues for the element-selective investigation and microscopy of magnetic materials.

In this paper we present a new multipurpose approach and instrument for magneto-optical spectroscopy and polarization analysis in the x-ray, EUV and visible region. The approach is designed to perform all above mentioned magneto-optical spectroscopy techniques over a broad photon energy range. The instrument includes a novel magnetization device, which produces tuneable magnetic fields up to 570 mT at the sample in all typical magnetization geometries. The versatility of x-ray magneto-optical polarization spectroscopy (XMAPS) is demonstrated for the example of a magnetic Co film with the focus on the Co $3p$ core levels. At these low binding energies that are accessible with EUV radiation the sample shows a reflectivity, which is at least two orders of magnitude larger than at the typically investigated high binding energies at the $2p$ edges. This leads to clear and well-pronounced magneto-optical reflection and polarization spectra. Some of them were obtained for the first time by using XMAPS. The observed magneto-optical spectra comprise rich magnetic information about the sample investigated and can be decomposed into bulk and surface contributions.

2. Theory

In this section the basics of magneto-optical spectroscopy techniques based on the photon-in–photon-out principle are outlined. Although the presented experimental setup allows for transmission, absorption and reflection spectroscopy including polarization analysis, we focus on the reflection and polarization spectroscopy. A detailed description of magneto-optical spectroscopy in transmission and absorption can be found in [1,3,11,20] and references therein. All magneto-optical spectroscopy techniques discussed require the use of polarized light. Therefore, the relevant parameters are briefly described in the following.

A. Polarized Light

For the description of the polarized light the electrical wave field is decomposed into two orthogonal components E_s and E_p that are perpendicular (E_s) and parallel (E_p) to the scattering plane. The field propagates in z direction with frequency ω, wave vector $\mathbf{q}$, and phase $\delta_{s,p}$ of these two components. The interaction of the light with a medium can be described by the complex coefficients of reflection $r_{s,p}$, transmission $t_{s,p}$, and phases δ_s and δ_p. Measurable quantities are the reflectance $R_{s,p}$, transmittance $T_{s,p}$ of the two components, and the phase retardation $\Delta = \delta_s - \delta_p$, that are given by [22–24]

$$\begin{aligned} R_{s,p} &= r_{s,p} r_{s,p}^*, \qquad r_{s,p} = |r_{s,p}| e^{i\delta_{s,p}} \\ T_{s,p} &= t_{s,p} t_{s,p}^*, \qquad t_{s,p} = |t_{s,p}| e^{i\delta_{s,p}} \\ \Delta &= \delta_s - \delta_p. \end{aligned} \tag{1}$$

The polarization of the light can be described by the Stokes vector $S = (S_0, S_1, S_2, S_3)$, where the Stokes' parameters can be expressed in terms of the components E_s and E_p by [23–25]:

$$\begin{aligned} S_0 &= [(E_p)^2 + (E_s)^2] \\ S_1 &= [(E_p)^2 - (E_s)^2]/S_0 \\ S_2 &= 2E_p E_s \cos(\delta_p - \delta_s)/S_0 = (E_s E_p^* + E_s^* E_p)/S_0 \\ S_3 &= -2E_p E_s \sin(\delta_p - \delta_s)/S_0 = (E_s E_p^* - E_s^* E_p)/S_0. \end{aligned} \tag{2}$$

The degree of linear polarization with respect to a fixed plane is described by S_1, while S_2 is the degree of linear polarization in a plane rotated by 45° with respect to the S_1 plane. The degree of circular polarization is given by $P_C = S_3$. The degree of linear polarization is given by $P_L = [S_1^2 + S_2^2]^{1/2}$ and the total degree of polarization P is given by $P = [S_1^2 + S_2^2 + S_3^2]^{1/2} \leq 1$. From these data the polarization ellipse with its axes a and b can be constructed. Its ellipticity ε and the tilt θ of the main axis a with respect to the polarization of the incoming light follow from

$$\sin 2\varepsilon = S_3 \tag{3}$$

$$\tan 2\theta = S_2/S_1. \tag{4}$$

The experimental analysis of the polarization state is described later in Section 3.

B. Polarization Spectroscopy in Reflection

The interaction of polarized light with a magnetic material can be described by several formalisms, which are equivalent and convertible into each other. The selection of the proper formalism depends on the individual scattering geometry as we will see below. A comprehensive description is achieved by the dielectric tensor $\boldsymbol{\varepsilon}$. Its elements refer to a preferred axis, e.g., the crystal axis or the magnetization direction of the matter and may be applied for transmission, absorption and scattering geometry [1,26]. From the dielectric tensor the magneto-optical index of refraction n (see Eq. (6) and discussion below) can be deduced. It completely characterizes the magneto-optical properties in a simple manner and it is suited for the description of transmission and Faraday experiments in terms of circularly polarized light [26]. It can be completely determined by a full polarization analysis of the light after its interaction with the magnetic sample. Reflection experiments can be simply described by appropriate reflection matrices, which are adapted to the individual reflection geometry. However, the objective of all individual and complementary descriptions, as outlined in the following, is the determination of magnetic information from the sample.

The principle interplay of the polarization and magnetization in elastic resonant scattering of polarized light of *isotropic*, magnetic matter can be well depicted by three terms which add up to the scattering amplitude f [1]

$$f \approx (\mathbf{e}' \cdot \mathbf{e})F_0 - i((\mathbf{e}' \times \mathbf{e}) \cdot \mathbf{M})F_1 + (\mathbf{e}' \cdot \mathbf{M})(\mathbf{e} \cdot \mathbf{M})F_2. \tag{5}$$

The polarization unit vectors, i.e., the electric field direction of the incoming and reflected light are given by $\mathbf{e}$ and $\mathbf{e}'$, respectively. The quantitative calculation of the scattering factors F_0, F_1 and F_2 can be found in [1]. The first and largest term in Eq. (5) comprises the charge contribution and is independent of the magnetization $\mathbf{M}$. The second term is linear in the magnetization. It is relevant for XMCD, Faraday effect, Kerr effect, L-MOKE, P-MOKE and T-MOKE experiments. In XMCD-experiments it scales with the degree of circular polarization and the scalar product $\mathbf{M} \cdot \mathbf{q}$ of magnetization $\mathbf{M}$ and light propagation vector $\mathbf{q}$ [1]. The third term is proportional to $(\mathbf{E} \cdot \mathbf{M})^2$ and thus even in $\mathbf{M}$. Largest values are obtained for parallel orientation between electric field $\mathbf{E}$ and the magnetic moment while the wave vector is perpendicular to $\mathbf{M}$. This term dominates the XMLD and Voigt-effect [15], which makes both spectroscopies suitable for the investigation of AFM samples. However, the determination of the scattering factors in Eq. (5) is not aim of this paper although these are related to the magneto-optical constants and reflection coefficients, which are presented in the following for the various scattering geometries.

C. L-MOKE

The longitudinal magneto-optical Kerr effect is observed for magnetic fields applied in the surface plane and lying parallel to the scattering plane [Fig. 1(a)]. Relevant for L-MOKE is the component of the magnetization along the light propagation direction, which means $\mathbf{M} \cdot \mathbf{q} \neq 0$. After interaction with the magnetic sample the polarization plane of linearly polarized light is rotated and its polarization changes to elliptical [Fig. 1(a)]. The underlying physical effect is identical to the Faraday effect observed in transmission. In both effects the incident linearly polarized wave is interpreted as the

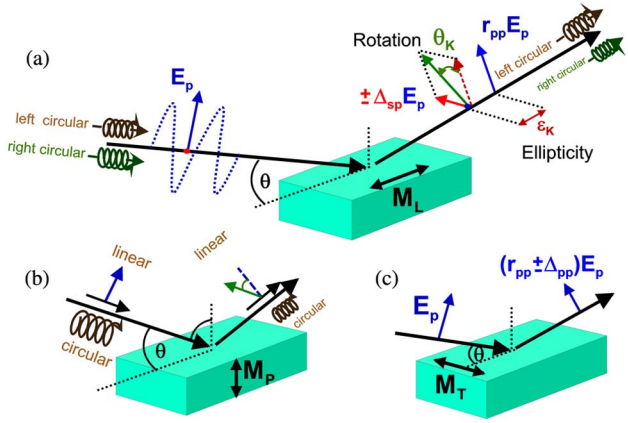

Fig. 1. Experimental geometries: (a) L-MOKE: rotation and change of ellipticity of linearly polarized light appears upon reflection on a longitudinally magnetized sample. This is detected by a polarization analysis (not shown). Circularly polarized light changes its intensity, depending on parallel/antiparallel orientation of helicity and magnetization direction. This is detected by XMCD reflectivity measurements. (b) P-MOKE: rotation of the polarization plane and change of the ellipticity of linearly polarized light appears upon reflection of polar magnetized samples. This is detected by a polarization analysis (not shown). A plain intensity measurement of circularly polarized light is called XMCD in reflection similar to situation (a). (c) T-MOKE: linearly *p*-polarized light impinges a transversally magnetized sample and shows a change in the reflected intensity only. A detailed description is found in Section 2.2.

superposition of two circularly polarized beams with opposite helicity ($S_3 = \pm 1$) and identical amplitude.

A proper description of the interaction with the magnetic material is given by the complex index of refraction n_+, where + and − refer to parallel and antiparallel orientation of the photon helicity and the magnetic moment of the sample. In the x-ray region where n is close to one it adopts the form [25]:

$$n_\pm = 1 - (\delta_0 \pm \Delta\delta) + i(\beta_0 \pm \Delta\beta). \tag{6}$$

The dispersion of unpolarized light is described by δ_0, the absorption by β_0. The dichroism $\Delta\delta$ in the real part of the refractive index leads to different phase velocities in the magnetized sample. After interacting with the sample this phase difference between the two circularly polarized waves leads to the rotation angle $\theta_{F,K}$ in Faraday or Kerr experiments, respectively, [16]. The dichroism $\Delta\beta$ in the imaginary part leads to different absorption of the left and right circularly polarized waves and thus to an ellipticity $\tan(\varepsilon_{F,K})$ of the outgoing beam. Therefore simple intensity measurements with circularly polarized light can be used to gain magnetic information. However, linearly polarized light is typically used and a full polarization analysis is applied to obtain both the rotation angle and the ellipticity. While Faraday experiments on transmission samples reveal directly all individual terms in Eq. (6) [11] the L-MOKE reflection experiment yields entangled terms only. These are found in an equation of the Kerr rotation and Kerr ellipticity of the reflected light, which can be expressed by the nonmagnetic reflection coefficients r_{ss} and r_{pp} and the magnetization dependent coefficient r_{ps} [26]

$$\theta_{Kp} + i\varepsilon_{Kp} = -r_{ps}/r_{pp} \approx \frac{-in_0 nQ}{(n^2 - n_0^2)} \frac{\cos\phi_i \tan\phi_t}{\cos(\phi_i + \phi_t)}. \tag{7}$$

The index p in the Kerr constants indicates the experimental geometry, i.e., the polarization plane of the incident linearly polarized light is parallel to the reflectivity plane as used in our experiments. The magnetic dichroism can be defined by the Voigt parameter Q which adopts for L-MOKE the form $Q = (n_+ - n_-)/(n \sin\phi_t)$ with $n = 1/2(n_+ + n_-)$. A simple correlation between Kerr constants and the optical constants as defined in Eq. (6) is not found. This is typical for experiments in reflection because the dependence on the angle of incidence and refraction enters Eq. (7). Note that we name the angle of incidence θ, measured to the surface in our experiments. According to conventional notations in optical textbooks the angle of incidence $\phi_i = 90 - \theta$ is measured to the surface normal. The angle ϕ_t describes the refraction of the light beam within the material, measured to the surface normal. Equation (7) may be used to calculate the Kerr spectra for different angles of incidence from known magneto-optical constants. However, it is not usable the other way around for the deduction of magneto-optical constants from one single Kerr spectrum. A disentanglement of the magneto-optical constants is possible only for several measurements with different angles of incidence. In particular the reflectance at the surface expressed by the optical constant n_0 of the nonmagnetic cap layer or by $n_0 = 1$ for vacuum superimposes the Kerr data (Eq. (7) and hampers a simple separation of magnetic and nonmagnetic information as will be discussed in Section 4. However, even without knowledge of the magneto-optical constants the Kerr rotation as well as the reflection coefficients (Eq. (7) serve as a measure for the magnetization state of the sample.

The reflection coefficients can be obtained from simple intensity measurements without any polarization analysis of the reflected light. To deduce them we consider the electric field $\mathbf{E}'$ of the reflected wave which is given by the product of the reflection matrix with the incoming wave $\mathbf{E} = (E_x, E_y)$ resulting in $\mathbf{E}' = \mathbf{r}\,\mathbf{E}$. The reflected intensity is given by $I'_\pm = (|E'_x|^2 + |E'_y|^2)$. For x perpendicular and y parallel to the reflection plane we obtain for L-MOKE [26]

$$\mathbf{r_L} = \begin{pmatrix} r_{ss} & \pm\Delta_{sp} \\ \mp\Delta_{sp} & r_{pp} \end{pmatrix}. \tag{8}$$

The terms $|r_{ss}|^2$ and $|r_{pp}|^2$ are identical to the nonmagnetic Fresnel reflectances R_s and R_p, respectively. The magnetic contribution to the reflectivity is comprised by Δ_{sp} where the signs $\pm$ refer to the parallel or antiparallel magnetization directions. Once these coefficients are known, every x-ray reflectivity experiment can completely be described. Simple intensity reflection experiments with fully circularly polarized light lead to the XMCD-reflection asymmetry parameter A_L in L-MOKE geometry where the signs $\pm$ refer to the parallel/antiparallel orientations between magnetization vector and direction of the circularly polarized light

$$\begin{aligned} A_L &= \frac{R_{L+} - R_{L-}}{R_{L+} + R_{L-}} \\ &= 2\,\mathrm{Im}\{-\Delta_{sp}(r_{ss} + r_{pp})\}/(|r_{ss}|^2 + |r_{pp}|^2 + 2|\Delta_{sp}|^2). \end{aligned} \tag{9}$$

For the case of elliptically polarized light, i.e., $S_3 \neq 1$, the degree of polarization and the polarizing power p_p of the investigated sample modify the asymmetry parameter as described by [27]

$$\begin{aligned} &A_L = (a_L S_3)/(1 - p_p(1 - S_3^2)^{1/2}) \\ &\text{with } a_L = 2\,\mathrm{Im}\{-\Delta_{sp}(r_{ss} + r_{pp})\}/(|r_{ss}|^2 + |r_{pp}|^2 + 2|\Delta_{sp}|^2) \\ &\text{and } p_p = (|r_{ss}|^2 - |r_{pp}|^2)/(|r_{ss}|^2 + |r_{pp}|^2 + 2|\Delta_{sp}|^2). \end{aligned} \tag{10}$$

These equations show that the measured asymmetry parameters can be split into two contributions. The magnetic asymmetry a_L is almost proportional to the magnetization while the polarizing power of the sample p_p is almost independent of the

magnetization. For circularly polarized light with $S_3 = 1$ we find $A_L = a_L$ because p_p vanishes in the denominator of Eq. (10). Using elliptically polarized light with $S_3 < 1$ a renormalization is required according to the polarizing power, which will be discussed in detail in Section 4.

D. P-MOKE

The polar magneto-optical Kerr effect is similar to the L-MOKE but with magnetization perpendicular to the sample surface [Fig. 1(b)]. The polarization plane of incident linearly polarized light is rotated and the polarization state changes to elliptically polarized due to the different reflection coefficients for the left and right circularly polarized components [Figs. 1(a)1(b)]. The typically small Kerr rotation and Kerr ellipticity can be expressed in terms of the magneto-optical constants $n_\pm$ for parallel and antiparallel orientation of the photon helicity and the magnetic moment [26]

$$\theta_{Ks} + i\varepsilon_{Ks} \approx \frac{i(n_+ - n_-)n_0}{n_+ n_- - n_0^2} \frac{\cos\,\phi_i}{\cos(\phi_i - \phi_t)} \tag{11a}$$

$$\theta_{Kp} + i\varepsilon_{Kp} \approx \frac{i(n_+ - n_-)n_0}{n_+ n_- - n_0^2} \frac{\cos\,\phi_i}{\cos(\phi_i + \phi_t)} \tag{11b}$$

with the index $s(p)$ for s-polarized (p-polarized) light, the angle of incidence ϕ_i and the angle of refraction ϕ_t measured to the surface normal and n_0 is the optical constant of the cap layer. For exact normal incidence both equations are identical.

E. T-MOKE

The transversal magneto-optical Kerr effect is observed with linearly polarized light in p-geometry and transversal magnetization [Fig. 1(c)] [26]. In contrast to P-MOKE or L-MOKE no rotation or change in the ellipticity of the reflected light is observed and a polarization state analysis is not necessary. Instead different reflection coefficients occur for opposite magnetization directions. According to the definitions in L-MOKE a reflection matrix appears which is given by [26]

$$\mathbf{r_T} = \begin{pmatrix} r_{ss} & 0 \\ 0 & r_{pp} \pm \Delta_{pp} \end{pmatrix}. \tag{12}$$

The terms $|r_{ss}|^2$ and $|r_{pp}|^2$ are identical to the nonmagnetic Fresnel reflectances R_s and R_p, respectively. The magnetic contribution to the reflectivity is expressed by Δ_{pp}, where the signs $\pm$ refer to the magnetization directions. From Eq. (12) the reflection coefficients R_+ and R_- for the two transversal magnetization directions are deduced leading to the asymmetry parameter

$$A_T = \frac{R_+ - R_-}{R_+ + R_-}. \tag{13}$$

Just as for L-MOKE the asymmetry parameter depends on the degree of linear polarization and much more on the polarization power p_T of the investigated sample as can be expressed by [27]

$$A = a_T(1+S_1)/(1-p_T S_1)$$
$$\text{with } a_T = 2\mathrm{Re}\{\Delta_{pp} r_{pp}\}/[|r_{ss}|^2 + |r_{pp}|^2 + |\Delta_{pp}|^2]$$
$$\text{and } p_T = (|r_{ss}|^2 - |r_{pp}|^2 - |\Delta_{pp}|^2)/(|r_{ss}|^2 + |r_{pp}|^2 + |\Delta_{pp}|^2). \tag{14}$$

This shows that a strong artificial enhancement of the characteristic magnetic contribution a_T is induced by the denominator $(1 - p_T S_1)$ in Eq. (14). The denominator decreases strongly toward the Brewster angle where p_T shows a maximum. As a result the measured asymmetry A_T is strongly enhanced over the characteristic magnetic contribution a_T around the Brewster angle, which will be discussed in Section 4. Note that T-MOKE can also be measured with circularly or even unpolarized light since in both situations the light contains a linearly p-polarized component.

F. XMLD in Reflection

X-ray magnetic linear dichroism has emerged as an important tool for the investigation of AFM materials because this spectroscopy is sensitive to the square of the magnetization as expected by the third term in Eq. (5). Typically the XMLD is observed with linearly polarized light in transmission or absorption by an intensity measurement, while the Voigt effect needs a polarization analysis of the light after its interaction with the magnetized sample [15,28,1] which leads to the complete set of relevant magneto-optical constants. Meanwhile a XMLD reflection spectroscopy has been developed which allows for surface sensitive and depth profiling spectroscopy of layered systems and buried AFM films due to the tuneability of the penetration depth of the incident light by varying the angle of incidence [28].

The scattering geometry is sketched in Fig. 2. The magnetization axis is in plane and linearly p- or s-polarized light is incident on the sample. The incidence angle is fixed and the reflectance is measured twice, first with parallel orientation ($R_\parallel$), second with perpendicular orientation ($R_\perp$) between magnetization axis and polarization vector. Therefore the magnetization axis needs to be rotated. This can be done experimentally by switching the external field for

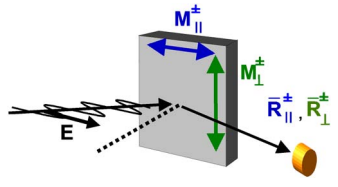

Fig. 2. Principle of detecting the XMLD. The reflectance $R_\parallel, R_\perp$ of the sample differs for the two magnetization directions $\mathbf{M}_\parallel$, $\mathbf{M}_\perp$ parallel and perpendicular to the electric field component $\mathbf{E}$ of the incident linear polarized light.

ferromagnetic samples or by rotating of the sample about its surface normal for AFM samples. A rotation of the polarization vector, while fixing the magnetization direction, is not allowed since it would change the scattering geometry from p- to s-polarized light or vice versa. The magnetic information is obtained from the asymmetry parameter [28]

$$A_{\mathrm{LD}} = \frac{R_{\parallel} - R_{\perp}}{R_{\parallel} + R_{\perp}} = \mathrm{Re}\left\{(\varepsilon_{\parallel} - \varepsilon_{\perp}) \frac{\cos\phi_i \cos\phi_t}{\bar{n}(\bar{n}^2 f_p - 1)} (\tan^2\phi_t + 1)\right\}. \quad (15)$$

The scaling factor contains the nonmagnetic refraction index $\bar{n}$ and $f_p = \cos^2\phi_i/\cos^2\phi_t$. The magneto-optical quantity of interest is $(\varepsilon_{\parallel} - \varepsilon_{\perp})$, where $\varepsilon_{\parallel}$, $\varepsilon_{\perp}$ are the components of the dielectric tensor that are parallel or perpendicular to the magnetization direction.

3. Experimental Setup

The experimental station for XMAPS is transportable and can be operated with visible light sources in the home laboratory as well as with synchrotron radiation at any facility. This station, shown in Fig. 3, comprises the vacuum chamber, the magnetization device, the polarization analyzer devices, intensity detectors and beam diagnostics. These components are described in detail in the following sections.

A. XMAPS: Chamber and Mechanics

The device consists of an ultra-high vacuum (UHV)-chamber of 600 mm diameter (Fig. 3). The light passes higher order suppression filters and pinholes for beam adjustment and monitoring devices (items b in Fig. 3). Available filters are 150 nm thick Al, 120 nm thick Si and a 120 nm thick Boron films. In the center of the chamber the light interacts with the sample, which is hold in the magnetization device *TetraMag* (part c in Fig. 3, Fig. 4).

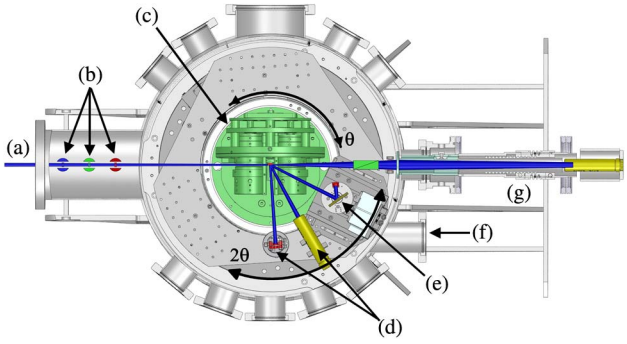

Fig. 3. Top view of the XMAPS chamber. The incident light (a) passes a set of pinholes, filters and monitoring devices (b) and is reflected (transmitted) by the sample in the middle of the magnetization device *TetraMag* (c) placed on a two circle goniometer. (d) The reflected (transmitted) light can be detected with photodiodes or photomultipliers, respectively. (e) The polarization state of light can be analyzed by a Rabinovich detector or (g) a Wollaston prism based detector. (f) The *in situ* sample transfer takes place via a transfer chamber mounted at position.

This is mounted on a noncommercial two-circle goniometer, which allows for rotation about a vertical axis, called theta-axis, to tune the angle of light incidence θ between grazing incidence at 0° to near normal incidence at 88°, each measured with respect to the sample surface. After reflection of the sample the beam can be detected (item d in Fig. 3) and/or its polarization state can be analyzed (items e and g in Fig. 3). The corresponding detectors (d, e) are mounted on the second circle of the goniometer and can be moved on the reflected beam by tuning the angle 2θ between 0° and 176°. The axes of the θ- and 2θ-tables accord within 0.28 mrad tilt and 50 μm shift. The 2θ-table is designed spaciously so that additional analyzing devices can be implemented if required in future. The angular step width and accuracy is better than 0.01° for both, θ and 2θ, respectively. The optical axis of the chamber has been prealigned with respect to orthogonal intersection of the theta-axis by standard adjustment procedures. The intersection accuracy is better than 0.1 mm and the orthogonality is better than 0.5 mrad. The position of the optical axis is fixed and defined in the chamber by the position of the entrance pinhole (item b in Fig. 3) and the position of a pinhole at the end of the chamber. Using these two pinholes the chamber can be aligned to the beam with a lateral accuracy of 50 μm and an angular accuracy of 0.5 mrad. A transfer-chamber with a sample magazine allows for an *in situ* sample exchange (item f in Fig. 3) of up to 5 different samples.

Detectors for the visible and UV range comprise Si-diodes with a detection range from 190 to 1000 nm (type S1227, Hamamatsu) and photo multiplier tubes. These have green enhanced bialcali photo cathodes on MgF_2 windows, which enable detection between 115 and 650 nm with a typical gain of $3 \cdot 10^6$ (type 9407, electron tube company). For the EUV- and soft x-ray range GaAs:P diodes without window are used (type G1747, Hamamatsu).

B. XMAPS: Light Sources

The setup is designed for a wide energy range from the visible up to the soft x-ray regime. It can be operated alternatively with synchrotron radiation at any beamline or with commercial light sources in the laboratory. For the range 200–2200 nm a 175 W xenon lamp is used with a monochromator (type Digikröm, 480 mm focal length) and two gratings (1220 lines/mm, blaze at 500 nm, 250 nm) giving a spectral width of up to $\Delta\lambda = 0.03$ nm. For the range from 115 to about 400 nm a 150 W deuterium lamp and a monochromator (type 234/302, McPherson, 200 mm focal length) and a holographic grating with 1200 lines per mm is used giving a spectral width of up to $\Delta\lambda = 0.1$ nm at 313.1 nm.

In the visible and UV region the incoming light is linearly polarized using Glan–Thomson polarization techniques [23], i.e., a rotatable MgF_2 cube with 15 mm × 15 mm active area. It creates a degree of

linear polarization better than $P_L = 0.999998$ and tunable orientation from horizontal p-polarization to vertical s-polarization. Synchrotron radiation shows a well-defined polarization state even without a polarizer [29] which can be tuned from linear to circular, depending on the beamline and undulator [30–32].

The synchrotron radiation experiments reported in this paper have been performed at the facility DELTA, a 3rd generation synchrotron maintained by the Center for Synchrotron Radiation of the TU Dortmund University. The bending magnet beamline no. 12 covers the energy range from 20 to 150 eV [33]. The degree of polarization was determined experimentally to $P_L = 0.91$ and $P_C = \sqrt{1 - P_L^2} = 0.41$ at 60 eV photon energy using the below described technique. The spectral resolution was set to $E/\Delta E = 300$. The undulator beamline U55 covers the energy range from about 60 to 1500 eV providing completely linearly polarized light [34] with horizontally oriented polarization plane, i.e., p-polarized light for our experiment. The energy resolution was set to $E/\Delta E = 1000$.

C. XMAPS: Polarization Analysis

In the visible and UV-region the polarization analysis is performed using a Wollaston MgF_2 prism with active area of 15 mm × 15 mm that splits the light into two beams (Fig. 5), one with s- and one with p-polarization with a suppression power of $I_s/I_p = 10^5$ resulting in $P_p \approx 1$. The individual beam intensities I_s and I_p of these two orthogonal polarization states are detected simultaneously with two photomultiplier tubes (Fig. 5).

The degree of linear polarization is deduced according to $P_L = (I_s - I_p)/(I_s + I_p)$. In Fig. 3 (item g) this polarization analyzer is shown at the position for analyzing the incoming beam without sample. For a polarization analysis of the beam after reflection from the sample the analyzer has to be mounted on one of the flanges aligned for fixed angles of reflection 2θ between 45° and 160°.

In the x-ray region the incoming or reflected beams are analyzed by a Rabinovich detector [23] (Fig. 3, item e and Fig. 6), which exploits a mirror operated at the Brewster angle. The mirror is rotated around the azimuthal angle γ while the reflected beam is monitored by a GaAs:P diode. For the energy range between 20 and 100 eV a gold mirror shows good performance [35]. For higher energies the gold mirror can be replaced by x-ray multilayer mirrors. These are designed such that Bragg angle and Brewster angle coincide for the selected photon energy. Typical implementations can be found in [36,37]. Both the Wollaston and the Rabinovich analyzers are rotated about γ via a commercial UHV compatible goniometer (type Huber 408) with an accuracy of 0.018 mrad. The Rabinovitch detector, which is mounted on this goniometer, is made up by a compact 50 mm large two-circle goniometer (Fig. 6).

This device allows for aligning (i) the mirror's incidence angle γ_θ on the photon energy dependent Brewster angle as well as (ii) the corresponding diode on the reflection angle $\gamma_{2\theta}$, each with an accuracy of 0.35 mrad. A special mechanical feature is the ability to align the complete Rabinovitch detector including the Huber 408 goniometer with respect to the light axis, i.e., the alignment of the γ axis and the axis of the investigated light.

D. XMAPS: Magnetization Device *TetraMag*

Commonly used magnetization devices involve solenoids, most often with soft iron yokes, which are arranged in dipole, quadrupole or octupole geometry, respectively, [38,39]. However, solenoids do not meet all of the following requirements of an ideal magnetization device: (i) tunable magnetic field strength, (ii) rotatable magnetic field direction in space, (iii) stable field with negligible ripple and homogeneous across the sample region of interest, and (iv) accessibility to the sample over a wide angular range, e.g., for scattering experiments. Ideally, the magnetic field can be tuned with negligible magnetic hysteresis and the thermal load should be negligible to facilitate the technical expenses. Last but not least UHV compatibility is desirable due to the increasing amount of experiments exploiting synchrotron radiation. An interesting technical alternative to solenoids is provided by permanent magnets with a high energy product, i.e., preferentially of the NdFeB or CoSm type. There exist various arrangements of magnets to create tunable and more or less homogeneous fields reaching from quadratic arrangements of rotatable magnetic cylinders [40,41] to more sophisticated designs like e.g., Halbach cylinders [42,43].

For XMAPS, we used a novel compact magnetizing device [44] based on a quadrupolar arrangement of eight diametrically magnetized NdFeB permanent magnets of cylindrical shape which are symmetrically arranged in two concentric squares, and which can be rotated with respect to each other about their individual length axes (Fig. 4). At the sample, placed in the center, the magnetic field contributions of all magnets are superimposed and add up to the

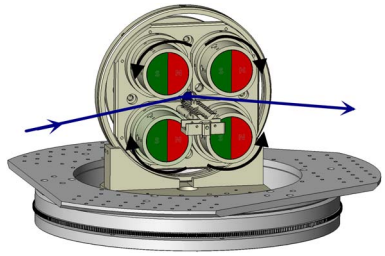

Fig. 4. Magnetization device *TetraMag* placed in the center of the two-circle goniometer. The light interacts with the sample in the center of the *TetraMag*. Four strong (north and south poles colored in green and red, respectively) and four weak (not shown) permanent magnets create a homogeneous field in the sample area that is tunable by rotating the magnets (black arrows).

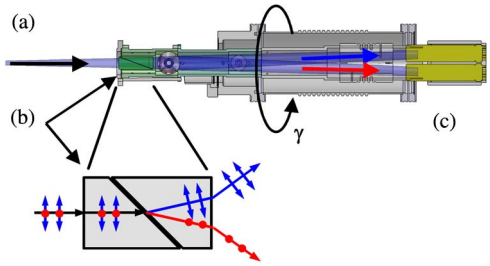

Fig. 5. Polarization detector based on a Wollaston prism. The incident light (a) is split by a Wollaston prism (b) in its *s*- and *p*-polarized components. These are detected separately by two photomultipliers (c). Rotation of the whole detector about γ allows for a full polarization analysis.

resulting magnetic field. The major field contribution arises from the strong magnets. The smaller magnets (not shown in Fig. 4) serve as field correctors to increase the field homogeneity at the sample position. In order to vary the magnetic field in magnitude each magnet can be rotated about its longitudinal axis. The magnetic field direction is maintained and the field strength is tuned from maximum positive field across zero to maximum negative field and back. This device, which due to its four pole piece geometry is called *TetraMag*, overcomes many of the technical problems of solenoid systems mentioned above. It creates stable and homogeneous magnetic fields at the sample position with a resolution of 0.02 mT tunable between −570 and +570 mT. The magnetic field strength B_x (horizontal orientation) and B_y (vertical orientation) at the sample position as a function of the relative

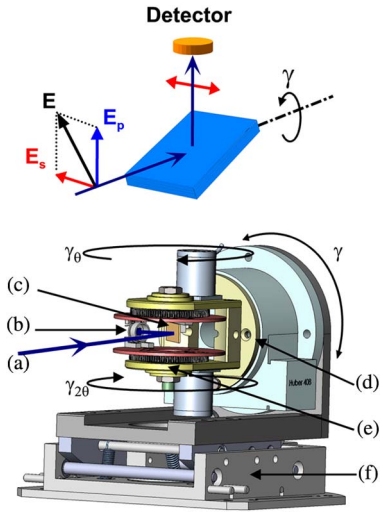

Fig. 6. Top: principles of the Rabinovich detector: *s*- and *p*-polarized light is separated exploiting the different reflectivity at the Brewster angle. Bottom: the incident light (a) is detected by a GaAs:P-photodiode (b) after reflection from the analyzer mirror (c) set to the Brewster angle. For a polarization analysis mirror and detector are rotated about the light axis (γ–scan) via a commercial goniometer (d). The mirror and the diode can be adjusted by a small noncommercial two-circle goniometer (e). A two axial bearing (f) provides easy alignment of the complete device with respect to the light axis.

rotation angle α of the magnetic rods is shown in Fig. 7(a).

A continuous variation of B_x is achieved between −570 and +570 mT. This field B_x is applied for longitudinal magnetization $\mathbf{M}_L$ [Fig. 1(a)] and $\mathbf{M}_\parallel$ (Fig. 2). By switching an internal mechanism *TetraMag* creates tunable vertical fields $-570\ \text{mT} \le B_y \le +570\ \text{mT}$ with $B_x = 0$. These are applied for T-MOKE [Fig. 1(c)] and for $\mathbf{M}_\perp$ (Fig. 2). P-MOKE [Fig. 1(b)] is realized with longitudinal B_x-fields but using a special type of sample holder which mounts the sample at near normal incidence. Hence, all desired scattering geometries can be realized.

The homogeneity of the magnetic field in the sample surface and along the field axis is depicted in Fig. 7(b). Best performance is obtained for intermediate field strengths, e.g., for 300 mT. A constant plateau of $B_x = 300\ \text{mT} \pm 2\ \text{mT}$ is observed between $-8\ \text{mm} < x < +8\ \text{mm}$, which is wider than the typical sample size of 10 mm × 10 mm. For larger as well as for very small magnetic fields the plateau of constant magnetic field strength is typically reduced to 4 mm × 4 mm which is, however, acceptable for practical applications. A detailed description of *TetraMag* can be found in [44].

4. Experimental Results

In this section the versatile usability of the XMAPS experimental chamber and approach is demonstrated by a considerable set of different magneto-optical reflection and polarization studies covering all above-mentioned scattering geometries.

The experiments were performed in the laboratory using the above-described visible and UV light sources to cover the interband transition range. At the synchrotron facility DELTA the bending magnet beamline no. 12 was used to cover the Co 3*p* edges and the undulator beamline no. 11 to cover the Co 2*p* edges. In all cases we used a sample comprising a polycrystalline 50 nm thick Co layer grown on an oxidized Si-wafer and with a 5 nm Cu cap layer. The Al-filter was used to prevent higher order components of the monochromator with a second-order suppression ratio of $I(60\ \text{eV})/I(120\ \text{eV}) = 100$ at the Co 3*p* edge.

A. Reflection Spectroscopy

1. T-MOKE

The absolute reflectivity across the 3*p* edge of the Co sample for an angle of incidence $\theta = 50°$ measured to the sample surface is shown in Fig. 8 (top). According to Fig. 1(c) two measurements were performed with transverse magnetic fields of $B_T = +10\ \text{mT}$ and $B_T = -10\ \text{mT}$ which ensure magnetic saturation in opposite directions. Two well-pronounced spectral structures with shoulders at the low and high energy sides are observed (Fig. 8, top). They are assigned to the oxidized near-surface region as will be discussed in Section 4.1.2 in detail. From these two reflection spectra the T-MOKE asymmetry A_T is deduced via Eq. (13) (Fig. 8 bottom). It reaches values of up to

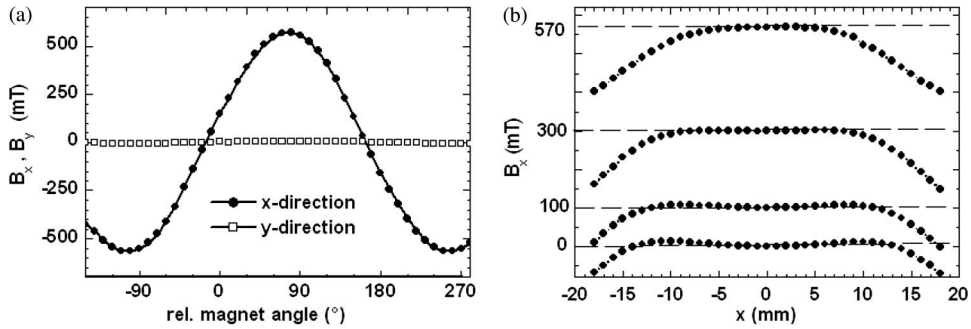

Fig. 7. Experimental data of (a) the magnetic flux density at the sample position depending on the angle of the magnets and (b) the magnetic flux density in x direction along the x axis in the sample plane for different field strengths.

25% at 61.3 eV and fades out below and above the 3*p* edge.

For the Fe 3*p* edge larger asymmetry values of up to 52% are reported at $\theta = 45°$ [45]. These increased values do not only arise from the increased magnetic moments showing a ratio of $\mu_{Fe}/\mu_{Co} = 1.3$ [1] but first of all from the influence of the angle of incidence. This can be demonstrated by the angular dependence of the T-MOKE reflectivity as shown for a fixed photon energy of 60.5 eV in Fig. 9. Two spectra from grazing incidence at 0° to near normal incidence at 80° are recorded with $B_T = +100$ mT and $B_T = -100$ mT, respectively, (Fig. 9, top), to deduce the asymmetry (Fig. 9, bottom). The maximum asymmetry does not appear at $\theta = 50°$, but rather at 42° and 56° and is a factor of two larger than at $\theta = 50°$. The Brewster angle of the investigated sample is in this angular range leading to a minimum reflectance for *p*-polarized light, which in turn results in large asymmetry values (Fig. 9, top). Therefore, a quantitative comparison of T-MOKE signals needs a precise specification of both the angle of incidence and photon energy. A more detailed discussion is given e.g., by [46,27].

According to the discussion of Eq. (14) a normalization of the asymmetry spectra A_T with respect to the polarizing power could be performed to obtain the characteristic magnetic term a_T. However, this is not done in this paper for the sake of comparability with spectra taken by other groups. A partial rescaling according to Eq. (14) with respect to the slightly reduced degree of linear polarization $S_1 = 0.91$ leads to a small increase of the peak value from $A_T = 0.25$ to 0.26.

As expected the asymmetry signal vanishes for angles near 0° and 90°. This angular dependence results from the scattering term $(\mathbf{e}' \times \mathbf{e}) \cdot \mathbf{M} \cdot F_1$ in Eq. (5). At the Brewster angle the electric field vectors of the *p*-polarized incident and scattered light are nearly perpendicular and the term $(\mathbf{e}' \times \mathbf{e})$ reaches a maximum absolute value. Additionally, the vector $(\mathbf{e}' \times \mathbf{e})$ is parallel to the transversal magnetic moment M resulting in a maximum product $(\mathbf{e}' \times \mathbf{e}) \cdot \mathbf{M}$. In contrast at both grazing and normal incidence the electric field vectors of the *p*-polarized incident and scattered light are nearly parallel, and with $(\mathbf{e}' \times \mathbf{e}) \approx 0$ also the magnetic signal disappears. The change of sign in the T-MOKE asymmetry near the Brewster angle is due to the scattering factor F_1 in Eq. (5). A detailed mathematical description is found in [1].

The resulting signal being an intensity asymmetry T-MOKE is well-suited for *in situ* recording magnetic hysteresis loops. Figure 10 shows the reflected intensity of *p*-polarized light as function of the transverse magnetic field strength between −300 mT and

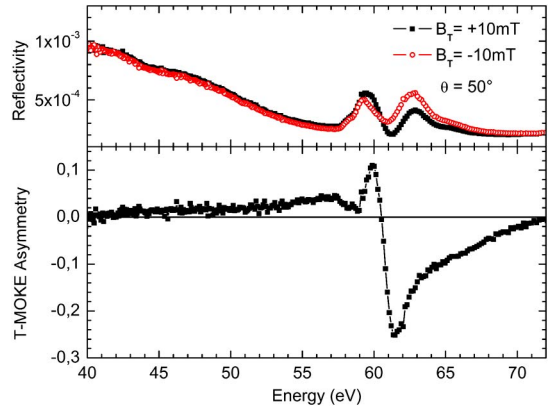

Fig. 8. Energy dependent reflectivity (top) at 50° incidence for transverse magnetic fields. The T-MOKE asymmetry (bottom) is deduced from the reflectance curves via Eq. (13).

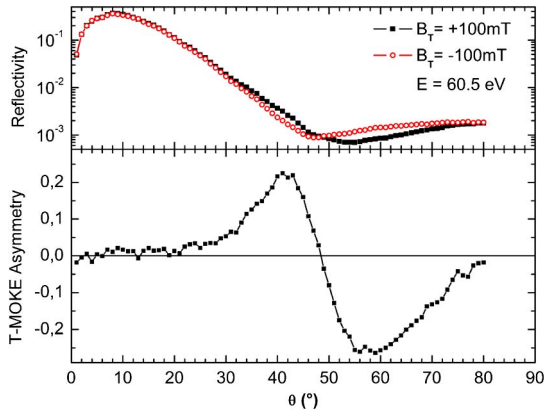

Fig. 9. Angular dependent reflectivity (top) at 60.5 eV for transversal fields. The corresponding T-MOKE asymmetry (bottom) is deduced from the reflectivity according to Eq. (13).

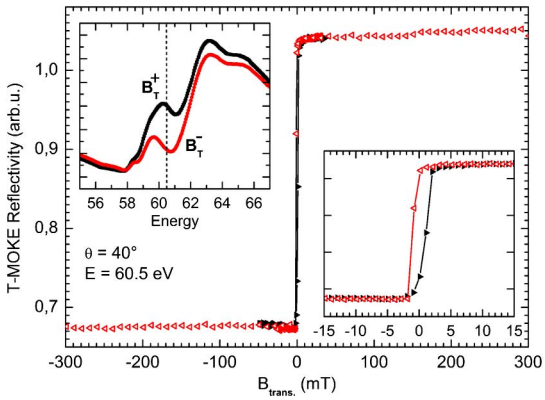

Fig. 10. Reflected intensity of Co as a function of the applied transversal magnetic field at 40° incidence. Maximum asymmetry appears at the 3*p* resonance near 60.5 eV (left inset). Right inset: details of the hysteresis loop.

+300 mT at fixed incidence angle $\theta = 40°$. The photon energy was set to 60.5 eV where the maximum asymmetry is observed in the reflection spectra (Fig. 10 inset left side). The inset (right side in Fig. 10) shows the details of the magnetic reversal giving a typical coercitivity of 2 mT. The shape of the hysteresis loop suggests that the magnetization reversal proceeds mainly via domain wall nucleation and propagation, with a small contribution from magnetization rotation at higher fields. This behavior is compatible with a soft polycrystalline magnetic film such as the Co film investigated.

For comparison the T-MOKE reflectivity across the high energy Co 2*p* edge is shown in Fig. 11 (top). Due to the low reflectivity, which is reduced by a factor of 100–1000 at these high photon energies compared to the 3*p* edge, spectra could be taken only up to a maximum angle of incidence $\theta = 15°$ to maintain a sufficient signal-to-noise ratio. The magnetic field was set to $B_T = \pm 450$ mT. The reflectivity shows a multiplet structure around the Co 2*p* edge with pronounced peaks at 786.7, 788.1, 789.6 and

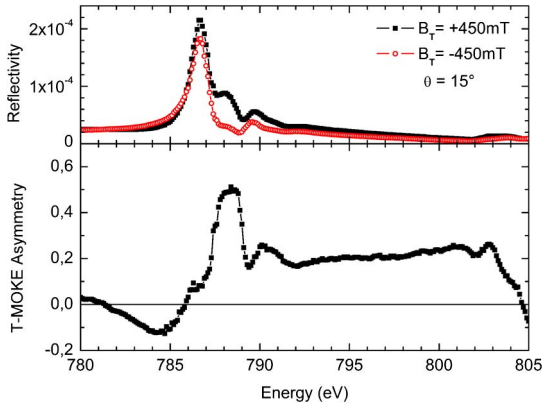

Fig. 11. Energy dependent reflectivity of Co across the 2*p* edges (top) at 15° grazing incidence for transversal magnetization. The $2p_{3/2}$ edge around 787 eV shows a multifold structure that is assigned to oxidation states. The corresponding T-MOKE asymmetry shows maximum values at the $2p_{3/2}$ edge near 788 eV and expands toward the $2p_{1/2}$ edge at ca. 803 eV.

792.4 eV. They can be assigned to states of oxidized Co and fit best to data obtained by photoelectron spectroscopy from Co_3O_4 [47,48]. The energy splitting between these four peaks found in reflection are 1.4, 1.5 and 2.8 eV, which agree well with those found for Co_3O_4 (1.3, 1.3 and 3.0 eV). We should point out that an additional contribution of CoO and hydroxide forms like CoOOH, which creates similar structures with splittings of 1.3 and 1.7 eV for the first three peaks, cannot be excluded [49].

The corresponding asymmetry signal (Fig. 11 bottom) reaches up to 50% at the 2*p* edge even at this small angle of incidence $\theta = 15°$. It is most pronounced at the high energy side of the $2p_{3/2}$ edge and expands toward the $2p_{1/2}$ edge around 803 eV. The asymmetry at the 2*p* edge is larger by a factor of two compared to the 3*p* region at $\theta = 50°$ (Fig. 8, bottom for $\theta = 50°$) and larger by a factor of three compared to results obtained at 30° (not shown). This increase may be assigned to the increased spin–orbit splitting of 15.2 eV at the 2*p* edge compared to the spin–orbit splitting at the 3*p* edges, which is less than 1 eV (see discussion later and [1,47]). Additionally, the information depth at the 2*p* edge is larger due to the increased penetration depth of light. Furthermore, the large spin–orbit splitting removes the partial overlap of m_J sublevels at the $p_{3/2}$ and $p_{1/2}$ levels which occurs at the 3*p* edge leading to different T-MOKE spectra at the 3*p* and 2*p* edges.

2. *L-MOKE*

In the L-MOKE geometry [Fig. 1(a)] we analyzed the polarization state of the reflected light (see Section 4.2.1) as well as the plain intensity variation, which leads to the longitudinal XMCD reflectivity asymmetry signal. For XMCD reflectivity measurements across the Co 3*p* edge the circularly polarized components of the elliptically polarized synchrotron radiation were exploited (Section 3.2). According to the geometry sketched in Fig. 1(a) the reflectivity was measured twice, first with parallel components of the magnetization direction and the light propagation direction and second with a component of the magnetization vector antiparallel to the light propagation. These two spectra are plotted in Fig. 12 (top) showing the same structures as for T-MOKE (Fig. 8, top), but a different magnetization dependence. This is clearly seen in the shape of the asymmetry curve deduced from these reflection spectra according to Eq. (9) (Fig. 12, bottom).

Due to the fact that these XMCD reflectivity measurements were not performed with fully circularly polarized light the measured asymmetry spectra have been rescaled according to Eq. (10) to obtain the asymmetry values that would be measured with fully circularly polarized light. To do so we used the experimentally determined degree of circular polarization $P_C = 0.41$, the amount of linear polarization $P_L = 0.91$ and the polarizing power of the Co sample ($0.92 < p_L < 0.97$) as calculated from optical constants [50] using the computer code REFLEC

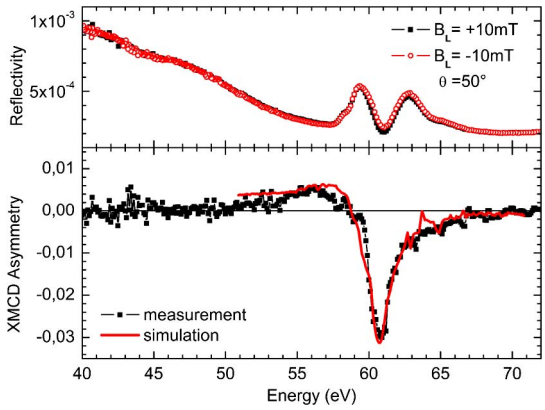

Fig. 12. Energy dependent reflectivity (top) of Co at 50° incidence for longitudinal magnetization. The longitudinal XMCD reflectivity asymmetry (bottom) is deduced from the reflectance according to Eq. (9). Symbols: experimental data; line: calculation based on magnetic Co in the volume and nonmagnetic CoO near the surface. For details see text.

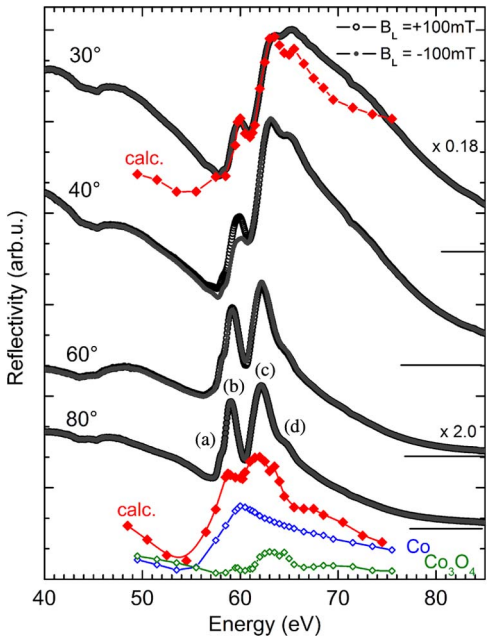

Fig. 13. Reflectance spectra for different angles of incidence for longitudinal magnetization (filled, open black circles). Structures (a) and (b) are assigned to metallic Co, structures (c) and (d) are assigned to oxidized Co in the near-surface region. The relative intensity of structures (c) and (d) increase from near-normal incidence ($\theta = 80°$) toward grazing incidence ($\theta = 30°$). Red filled diamonds: modeled spectra composed of pure metallic Co (blue open circles [54]) and Co_3O_4 (open green circles [57]). For details see text.

[51]. The rescaled spectrum is plotted in the bottom of Fig. 12 (symbols).

One important feature of the XMAPS experimental device is the possibility to record reflection spectra at any angle of incidence. By scanning the angle of incidence the depth profile of chemical or magnetization states in the sample can be determined, which allows separating near-surface signals from volume signals.

This is demonstrated in Fig. 13 (open and filled black circles). At near-normal incidence ($\theta = 80°$) the spectrum exhibits two well-pronounced structures (b) and (c) with one shoulder (a) at the low energy side and one shoulder (d) at the high energy side. Going toward grazing incidence ($\theta = 30°$) the structures (c) and (d) clearly grow in comparison to the low energy structures (a) and (b). Therefore the structures (a) and (b) are assigned to the bulk of the Cofilm while the structures (c) and (d) are assigned to the interaction of light with the surface-near region. The structures (c) and (d) are not induced by the 3 nm thin Cu cap layer because Cu does not show any core level structure in the Co 3*p* energy region [50]. Assuming a nonperfect Cu-cap layer the surface-near region comprises oxidized Co, producing the structures (c) and (d) while the structures (a) and (b) are assigned to nonoxidized Co in the volume. This interpretation is supported by the fact that the magnetic asymmetry is found most pronounced for the low energy structures (a) and (b) but negligible for (c) and (d) (see spectra with open/filled symbols for $\theta = 40°$ in Fig. 13). Both oxidation states, CoO and Co_3O_4 are AFM with a Néel temperature of 291 K [52] and 40 K [53], respectively. Therefore no significant magnetic contributions to the magneto-optical spectra are expected from surface near signals.

The thickness of the oxidized Co region can be estimated from the sampling depth of the light and is calculated from the absorption constant of the material [50]. For pure metallic Co this is $\alpha = 0.115\ \text{nm}^{-1}$ at the 3*p* edge, for oxidized Co the values change slightly by about 10%. The absorption constant of the oxidized Cu cap layer at the Co 3*p* edge is about $0.082\ \text{nm}^{-1}$ [50]. By tuning the angle of incidence the penetration depth of light in Co at the absorption edge decreases from $1/\alpha = 5.0$ nm at $\theta = 80°$ to $1/\alpha = 0.8$ nm at $\theta = 30°$. Thus, the thickness of the oxidized Co is roughly estimated to be in the range of 1–5 nm. For comparison, the penetration depth of light at the 2*p* edge is about 17 nm. Therefore with the 2*p* edge (Fig. 11) the Co bulk region is probed, while with the 3*p* edge the near-surface region is probed.

In the following we want to discuss the peaks (a–d) in more detail. Pure metallic Co typically shows one single peak near 59 eV in absorption spectra [54,55]. In contrast, both CoO and Co_3O_4 exhibit multiplet structures with 3 dominant peaks at photon energies above 59 eV in absorption spectra [56–60]. The structures emerge from the t_{2g} and e_g states, resulting from the crystal field splitting of Co^{2+} or Co^{3+} in the tetrahedral octahedral environment of oxygen ligands [57,61] and excitation to the oxygen ligands [56,57]. In particular the pronounced structures (b), (c), and (d) and their splitting energies ($E_b - E_c = 2.9 \pm 0.1$ eV, $E_c - E_d = 2.5 \pm 0.1$ eV) in our reflectance spectra are in good agreement with values observed in Ref. [56–58] ($E_b - E_c = 3.0 \pm 0.2$ eV, $E_c - E_d = 2.3 \pm 0.2$ eV) and those in Ref. [59] ($E_b - E_c = 2.9 \pm 0.2$ eV, $E_c - E_d = 2.1 \pm 0.2$ eV). The weak structure (a) at the low energy side of our

reflection spectra (Fig. 13) is split by $E_a - E_b = 0.9 \pm 0.1$ eV. A similar structure occurs in [59] with $E_a - E_b = 0.8 \pm 0.2$ eV and in [60] with $E_a - E_b = 0.9 \pm 0.2$ eV.

To understand qualitatively the origin of these four structures we model our spectra (Fig. 13) as the sum of one single peak of metallic Co at 59 eV [54] (Fig. 13, bottom, open blue circles) and a spectrum of Co_3O_4. The first weak peak of Co_3O_4, lying at 59 eV overlaps directly with the strong peak of metallic Co resulting in the modeled spectrum in one single peak at 59 eV. The next peaks of Co_3O_4 appear at 61.9 and 64.5 eV [57] (Fig. 13, bottom, open green diamonds). These two dominant peaks give rise to the features (b) and (c), which are split by 2.9 eV. At normal incidence the Co signal is weighted with 0.67, the Co_3O_4 signal is weighted with 0.33 giving the resultant spectrum (Fig. 13 bottom, filled red diamonds). At grazing incidence ($\theta = 30°$) the contribution of metallic Co to the total spectrum is reduced to a weight of 0.21 and the contribution of CoO [56] is increased to 0.79. The resultant spectrum is plotted in Fig. 13, top, red filled diamonds. This simple model does not produce a perfect fit but it shows the tendency when going from normal to grazing incidence and it reproduces the positions of the structures (b), (c), and (d) reasonably well.

The splitting of $\Delta = 0.9$ eV between the structures (a) and (b) which belong to metallic Co are assigned to the spin–orbit splitting of the Co $3p_{3/2}$ and $3p_{1/2}$ states which is in good agreement with findings of $\Delta = 1.0$ eV in [62].

Our simple model can also reproduce the XMCD reflectivity asymmetry (Fig. 12, bottom, line). The reflection signal from magnetic Co is set near 59 eV. The signal from nonmagnetic oxidized Co surface layer is shifted by 2.9 eV to higher energies. This shift corresponds to the splitting of structures (b) and (c) in our reflection spectra and to the corresponding splitting of 2.9 eV in the spectra of oxidized Co [56–58]. Using the program *ReMagX* [63] the XMCD reflectivity signal is computed, reproducing the experimental data quite well (Fig. 12, bottom). The computer code *ReMagX* gives best fits for a thickness of 5 nm of the nonmagnetic oxidized near-surface region.

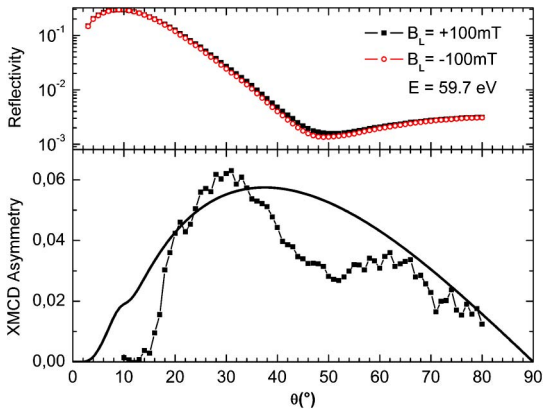

Fig. 14. Top: angular dependent reflectivity of Co at 59.7 eV in longitudinal geometry. The XMCD reflectivity asymmetry (bottom, points) is deduced from the reflectivity according to Eq. (9). The line shows the expected angular dependence (details see text).

The angular dependence of the reflectivity for a fixed photon energy at the $3p$ edge is plotted in Fig. 14 (top). The asymmetry, rescaled according to Eq. (10), is shown in Fig. 14 (bottom, points). The asymmetry signal increases toward an angle of 30° and vanishes close to 0° and 90°. This behavior is in accordance with observations at the high energy $2p$ resonances in Fe [27]. A similar behavior was also found by Höchst *et al.* for Fe [64,65]. A maximum in the asymmetry in the range between 20° and 30° results from the interplay of two terms: (i) the projection of the light propagation vector, which is for small scattering angles approximately parallel to $\mathbf{e}' \times \mathbf{e}$ and the magnetization $\mathbf{M}$ resulting in $(\mathbf{e}' \times \mathbf{e}) \cdot \mathbf{M} \sim \cos\theta$ and (ii) the interaction of the light with the magnetized Co sample. The second part is estimated by the transmittance of the Cu cap layer and the Cu/Co interface. The calculation of the transmittance has been done with the computer code REFLEC [51]. The product of the calculated transmittance and the $\cos\theta$ term is shown in Fig. 14 (bottom, line). A coarse agreement is found with some deviation at grazing incidence angles probably induced by the influence of stronger reflectance due to the nonmagnetic Cu cap layer.

3. *P-MOKE*

The P-MOKE intensity measurement is performed close to normal incidence at $\theta = 75°$ according to Fig. 1(b). These polar XMCD reflectivity measurements are possible due to the circular components in the elliptically polarized light, similar to that discussed in Section 4.1.2 for L-MOKE. Due to the incidence angle of $\theta = 75°$ for P-MOKE geometry the applied magnetic field was tilted by 15° with respect to the surface normal so that the direction of the external field was parallel to the incoming light. As a result the polar component, i.e., the magnetization perpendicular to the sample surface is given by $\cos(15°) = 0.97$ and a non-negligible longitudinal component appears with a weight of $\sin(15°) = 0.26$. Both contributions account for the reflectance spectra, which are plotted in Fig. 15 (top). In principle the physical origin of the asymmetry spectra for polar magnetization is similar to that observed for longitudinal magnetization. In both geometries the parallel components between magnetization and propagation direction of circularly polarized light are crucial. In our setup the main contribution in the XMCD reflectivity asymmetry in P-MOKE geometry arises from the polar field. The asymmetry shows a typical double lobe structure with zero crossing at 62.8 eV (Fig. 15, middle part). Positive values occur below the Co $3p$ resonance and negative values occur above the Co $3p$ resonance. The broad maximum below 62.8 eV is reduced by a strong negative peak at 60.8 eV. This feature arises from the contribution

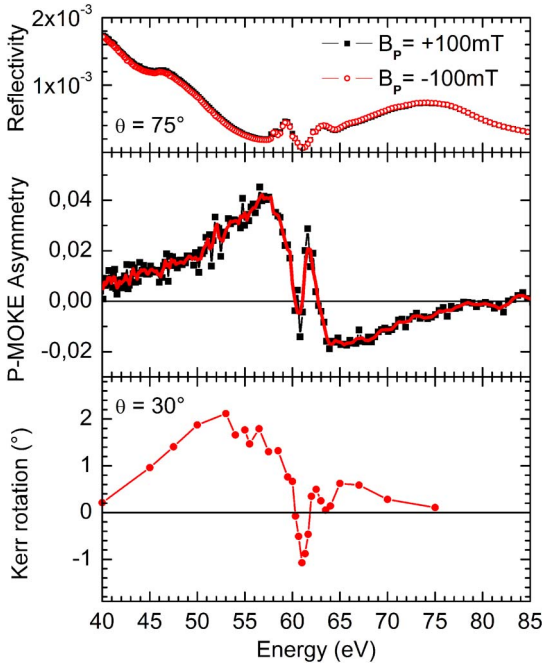

Fig. 15. Top: reflectivity spectrum of Co at 75° for polar magnetization. Middle: P-MOKE asymmetry calculated from the two reflectivity curves. Bottom: polar Kerr rotation deduced from polarization analysis at 30° grazing incidence.

of the L-MOKE asymmetry (Fig. 12, bottom), which shows negative sign and thus must be subtracted from the positive P-MOKE signal.

This interpretation is supported by the agreement in position and line width of both structures, i.e., the longitudinal XMCD reflectivity asymmetry and the dip in the polar XMCD reflectivity asymmetry. Even for pure XMCD reflectivity asymmetry in P-MOKE geometry, i.e., without any longitudinal field component, a difference between XMCD reflection spectra for polar and longitudinal field are expected due to the different angular behavior. This is also reported for the 3*p* edge of Fe [65].

4. *XMLD*

The XMLD-spectrum and thus the term in Eq. (5) that is quadratic in the magnetization $\langle \mathbf{M}^2 \rangle$ is deduced from two reflectivity spectra $R_{\parallel,\perp}$ with parallel and perpendicular orientation of the sample magnetization with respect to the polarization vector of the incoming light (see Fig. 2). For ferromagnetic materials like Co additional terms that are linear in the magnetization $\langle \mathbf{M} \rangle$ can appear in the XMLD spectrum. To avoid this contribution the reflectance is measured for two antiparallel magnetization directions $\pm\mathbf{M}$, and, subsequently by replacing $R_{\parallel,\perp}$ in Eq. (15) by the average values $(R_{\parallel,\perp}(+\mathbf{M}) + R_{\parallel,\perp}(-\mathbf{M}))/2$. These average reflectivity spectra are shown in Fig. 16 (top). The XMLD asymmetry deduced from the reflectivity according to Eq. (15) is shown in the bottom part of Fig. 16. To our knowledge this is the first reported XMLD spectrum at the Co 3*p* edge while data already exist for the Fe 3*p* edge [66]. Our XMLD

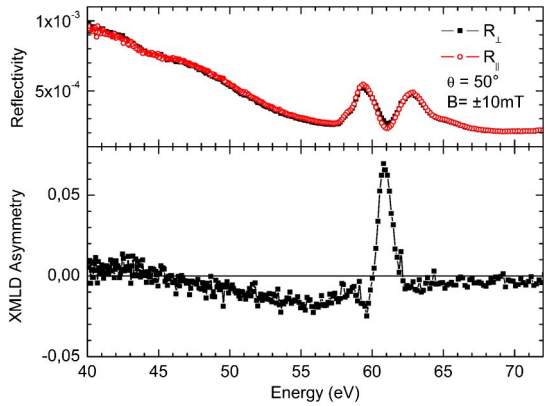

Fig. 16. Reflectivity (top) at the Co 3*p* edge at 50° incidence for two orientations between magnetization and polarization of the incident light: perpendicular ($R_\perp$) and parallel ($R_\parallel$). The XMLD asymmetry is deduced from the two reflectivity spectra according to Eq. (15).

spectra show a clear multiplet structure around the Co 3*p* edge, which shows similar characteristics as the finding for Fe [66]. However, the peak values of our data are larger by a factor of 10 compared to the Fe data [66]. This may be assigned to the influence of states arising from oxidized Co. A detailed explanation may be deduced from future band structure calculations.

The XMLD spectrum at the high energy Co 2*p* edge for a grazing incidence angle 15° is shown in Fig. 17. It agrees with the finding reported by Oppeneer *et al.* [28]. When comparing the spectra at the 2*p* and 3*p* core levels one must consider that the XMLD effect arises due to the interaction of the spin-polarized 3*d* electrons with the 3*p* core electrons, which creates an exchange splitting of the 3*p* and 2*p* levels [15]. Obviously, one should expect different XMLD line shapes for 2*p* and 3*p* edges. An increased number of structures at the 3*p* edge may arise from the small spin–orbit splitting of the $p_{3/2}$, $p_{1/2}$ states of about 1 eV, while it is about 15 eV at the 2*p* edge. As a result the exchange splitting of the $p_{3/2}$ and $p_{1/2}$ states,

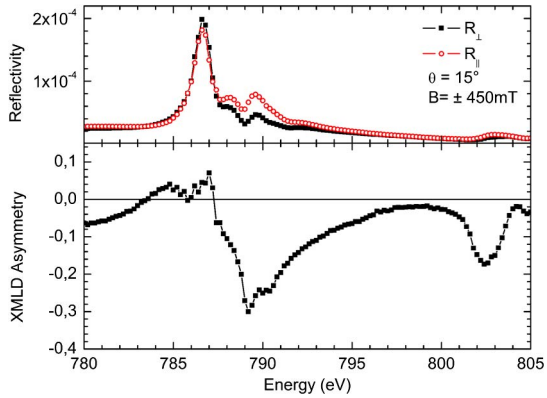

Fig. 17. Reflectivity (top) at the Co 2*p* edge at 15° grazing incidence for two orientations between magnetization and polarization of the incident light: perpendicular ($R_\perp$) and parallel ($R_\parallel$). The XMLD asymmetry is deduced from the two reflectivity spectra via Eq. (15).

which is in the order of 0.3 eV, would create a set of closely spaced levels at the 3*p* edge. In contrast, at the 2*p* edge the exchange split $p_{3/2}$ states and the exchange split $p_{1/2}$ states are well separated by the spin–orbit splitting which is nearly 50 times larger than the exchange splitting. This should lead to a smaller number of structures in the XMLD spectra at the individual $p_{3/2}$ and $p_{1/2}$ edges, respectively. This point could be proved by *ab initio* calculations. At present, however, such calculations are missing for the Co 3*p* edge, while some data are available for the Fe 3*p* edge [66]. Furthermore, comparative calculations and additional measurements for pure Co and oxidized Co are needed.

B. Polarization Analysis

Figure 18 shows the principle of a polarization analysis. The Kerr-rotation angel θ_K and the Kerr-ellipticity ε_K can be derived by taking two spectra, one of the incident light and one of the light after its interaction with the magnetized sample. The normalized angular intensity distribution of the incident beam as a function of the analyzer angle γ shows maximum intensity at $\gamma = 0°$ and minimum intensity at $\gamma = 90°$ corresponding to a horizontal polarization plane.

The polarization state of the analyzed light is deduced from a fit to the intensity distribution given by $I(\gamma) = I_0(1 + P_L P_p \cos 2(\gamma + \theta_K))$ with fit parameters I_0, the degree of linear polarization P_L and the Kerr rotation angle of the polarization plane θ_K. The analyzing power P_p of the rotating gold mirror has been calculated independently for each photon energy using the optical constants and the REFLEC code [51]. Across the Co 3*p* edge values of P_p between 0.91 and 0.92 have been found for the Brewster angle at 49°. The incoming light is completely linearly polarized. After inserting a longitudinally magnetized sample the polarization plane of the reflected light is rotated by θ_K, which can be directly observed by the shift of the signal (Fig. 18). In addition the ellipticity of the reflected light changes as seen by the reduced modulation depth of the analyzer spectrum (Fig. 18). The ellipticity ε_K can be obtained from fitting Eq. (3) to the data.

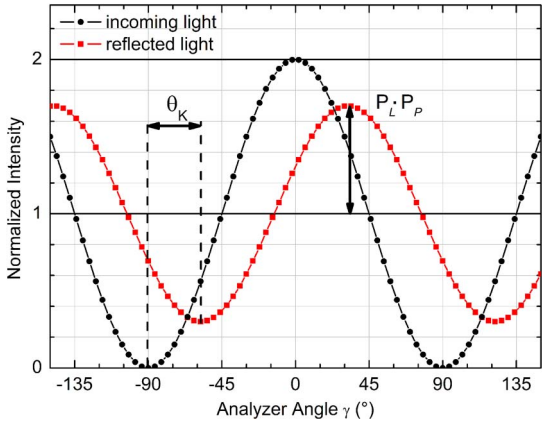

Fig. 18. Polarization analyzer spectrum. After reflection or transmission the signal (red) is phase shifted and of lower amplitude compared to the incoming signal (black). The phase shift contains information about the rotation θ_K of the polarization plane and the stroke contains information about the ellipticity ε.

1. Kerr Rotation (L-MOKE)

Several of the above described γ-scans (Fig. 18) have been measured across the 3*p* edge of the longitudinally magnetized Co sample [Fig. 1(a)] to determine the Kerr rotation and ellipticity spectra for *p*-polarized light incident at $\theta = 30°$. The Kerr rotation and the ellipticity are shown in Fig. 19 (bottom) and the corresponding reflectance for transversal magnetization in Fig. 19 (top). The rotation angles show a double lobe structure with peak values of up to 3°. Similar Kerr rotation spectra have been observed at the Fe 3*p* edge for incidence angles near $\theta = 30°$ [67]. Iron shows increased rotation values of 4°–5° which is accounted for by the 1.3 times larger magnetic moment of Fe compared to Co [1].

For the visible photon energy range the Kerr rotation decreases to small values around 0.1° (Fig. 20) in agreement with previous reports on Co and Cosystems [68–70].

At the high energy Co 2*p* edge huge Kerr rotation angles between 8° and 25° are detected [13]. A similar trend has been observed for Faraday experiments for Fe, Co and Ni transmission samples at the respective 2*p* edges [11] and 3*p* edges [71]. While small Faraday rotation angles are observed in the visible range [72], large Faraday rotation constants are obtained at the 3*p* edge with 2.1×10^5 deg /mm, 1.5×10^5 deg /mm and 0.8×10^5 deg /mm for Fe, Co and Ni, respectively, [71]. At the 2*p* edge the reported values are 2.3×10^5 deg /mm for Fe and Co [11]. As mentioned above this enhancement of the x-ray magneto-optical effects for higher photon energies is explained by the strong spin–orbit coupling for the 2*p* and 3*p* states in connection with the intense $2p - 3d$ and $3p - 3d$ excitations.

According to the outline in [13] the Kerr rotation and T-MOKE spectra are correlated. For *p*-polarized

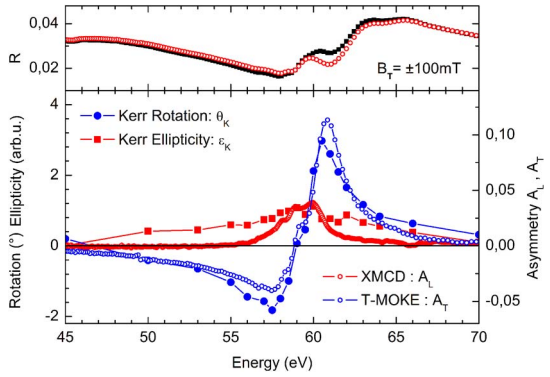

Fig. 19. Bottom: L-MOKE rotation and ellipticity spectra at 30° incidence (filled symbols) and T-MOKE and longitudinal XMCD reflectivity asymmetry (open symbols). Top: reflectivity spectra for transversal field at 30° incidence, from which the T-MOKE asymmetry A_T (bottom) was deduced.

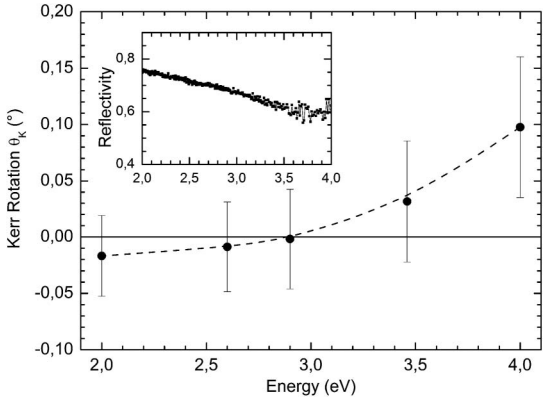

Fig. 20. L-MOKE rotation of Co in the visible region for s-polarized light at $\theta = 33°$. The reflectivity of Co is shown in the inset.

light the approximation $\theta_K \approx A_T \,\mathrm{Re}\{n_0/4\sqrt{n^2 - n_0^2} - \cos(\phi_i)/4\}$ should hold. The scaling between the T-MOKE asymmetry A_T and the Kerr rotation is given be the real part of a complex factor, which contains the average nonmagnetic optical constant n of the material, the optical constant n_0 of the nonmagnetic cap layer and the angle of incidence ϕ_i, measured to the surface normal.

This was first observed at the Co $2p$ edge [13] and now also at the Co $3p$ edge (Fig. 19, bottom). Both, Kerr rotation and T-MOKE asymmetry are recorded for identical incidence at $\theta = 30°$. The agreement shows that polarization analysis could be substituted by simple intensity measurements if the optical constants are known.

A similar relationship between the longitudinal XMCD reflectivity asymmetry and the Kerr ellipticity of p-polarized light is expected as expressed in [13] by $\varepsilon_K \approx 0.5 A_C + \cos\,\phi_i \,\mathrm{Im}\{r_{sp}\sqrt{n^2 - n_0^2}/n_0 r_{pp}^2\}$. Indeed this relationship is observed at the Co $2p$ edge, too. At the Co $3p$ edge a less pronounced agreement is observed (Fig. 19, bottom). Due to the offset given by the imaginary part in the equation the deviation between Kerr ellipticity and longitudinal XMCD reflectivity asymmetry is larger than for the Kerr rotation and the T-MOKE asymmetry.

A general aspect should be mentioned. In contrast to magneto-optical effects like Faraday or XMCD, which are observed in transmission or absorption, the reported reflection magneto-optical effects like Kerr-rotation or T-MOKE intensity spectra are strongly influenced by the reflectance behavior of the sample surface, in particular the coating layers which may induce interference effects. Therefore a straight-forward calculation of the magneto-optical constants from Kerr rotation or Kerr ellipticity is not as easily possible as for experiments in absorption or transmission [11]. In particular thin coatings and layer systems can create interference structures in reflectance and Kerr spectra, which sensitively depend on the angle of incidence [14], this has to be taken into account for a comparison of peak values with other measurements. Multiple reflections at interfaces, however, should not be topic of this paper. A detailed description of those effects can be found e.g., in [73,74].

2. *Kerr Rotation (P-MOKE)*

The Kerr rotation spectrum across the Co $3p$ edge for polar magnetization geometry is shown in Fig. 15 (bottom). To our knowledge these are the first published data. The rotation reaches maximum values of up to 2°, which is comparable to that observed for longitudinal magnetization (Fig. 19, bottom). In contrast to the rotation in longitudinal geometry the P-MOKE rotation shows a dip at 63 eV. This feature has been assigned to the nonperfect polar magnetic field and the influence of longitudinal components. A corresponding discussion has already been given in Section 4.1.2.

5. Conclusion

We presented the UHV compatible multipurpose chamber for XMAPS based on a novel magnetization device. It is dedicated to magneto-optical spectroscopy in a broad energy range from the visible to the soft x-ray regime. It enables intensity measurements in reflection, transmission and absorption as well as polarization analysis of the light after its interaction with the sample. All desired magneto-optical scattering geometries, such as longitudinal, transversal and polar can be realized. The XMAPS chamber is a versatile device, which allows for fast switching between all desired experimental scattering geometries as well as fast switching between intensity and polarization measurement. Thus, this device is best suited for the characterization of industrial samples, which typically are investigated in reflection spectroscopy. The versatility of XMAPS is demonstrated by recording the complete set of magneto-optical data in T-MOKE, L-MOKE, P-MOKE, XMLD, XMCD in reflection, as well as in Kerr-polarization spectra of a magnetic Co film across the Co $3p$ and Co $2p$ regions. Among these the P-MOKE rotation and the XMLD spectra at the $3p$ edge were presented for the first time. Furthermore, the XMAPS experimental device allows recording reflection spectra at any angle of incidence and thus acquiring of depth profiles of the sample. This feature enabled the separation of signals stemming from the oxidized near-surface region and pristine volume signals. In combination with future *ab initio* calculations for pure and oxidized Co the comparison of XMLD spectra at the $3p$ and $2p$ edge of $3d$ transition metals may give insight in the physical role of the relevant exchange interaction and spin–orbit interaction similar to recent investigations on Fe.

We thank C. Keutner for assistance at DELTA and O. Berges for construction and maintenance of the experimental set up. We acknowledge E. Goering and S. Macke for providing the computer tool ReMagX. This project was supported by the Ministry

for Innovation, Science and Technologies, NRW (INST 232/5-1).

References

1. J. Stöhr and H. C. Siegmann, in *Magnetism*, Springer Series in Solid State Sciences, (Berlin Heidelberg, 2006), pp. 351–468.
2. K. H. J. Buschow, in *Handbook of Magnetic Materials* Vol. **19** (North-Holland, Amsterdam, 2011) pp. 1–283.
3. C. T. Chen, Y. U. Idzerda, H.-J. Lin, N. V. Smith, G. Meigs, E. Chaban, G. H. Ho, E. Pellegrin, and F. Sette, "Experimental confirmation of the x-ray magnetic circular dichroism sum rules for iron and cobalt," Phys. Rev. Lett. **75**, 152–155 (1995).
4. J. B. Kortright, D. D. Awschalom, J. Stöhr, S. D. Bader, Y. U. Idzerda, S. S. P. Parkin, I. K. Schuller, and H.-C. Siegmann, "Research frontiers in magnetic materials at soft x-ray synchrotron radiation facilities," J. Magn. Magn. Mater. **207**, 7–44 (1999).
5. M. Sacchi and A. Mirone, "Resonant reflectivity from a Ni(110) crystal: magnetic effects at the Ni 2*p* edges using linearly and circularly polarized photons," Phys. Rev. B **57**, 8408–8415 (1998).
6. S. S. Dhesi, G. van der Laan, E. Dudzik, and A. B. Shick, "Anisotropic spin–orbit coupling and magnetocrystalline anisotropy in vicinal co films," Phys. Rev. Lett. **87**, 067201 (2001).
7. H. A. Dürr, E. Dudzik, S. S. Dhesi, J. B. Goedkoop, G. van der Laan, M. Belakhovsky, C. Moduta, A. Marty, and Y. Samson, "Chiral magnetic domain structures in ultrathin FePd films," Science **284**, 2166–2168 (1999).
8. P. Fischer, T. Eimüller, G. Schütz, G. Schmahl, P. Guttmann, and G. Bayreuther, "Magnetic domain imaging with a transmission x-ray microscope," J. Magn. Magn. Mater. **198–199**, 624–627 (1999).
9. F. Nolting, A. Scholl, J. Stöhr, J. W. Seo, J. Fompeyrine, H. Siegwart, J.-P. Locquet, S. Anders, J. Lüning, E. E. Fullerton, M. F. Toney, M. R. Scheinfein, and H. A. Padmore, "Direct observation of the alignment of ferromagnetic spins by antiferromagnetic spins," Nature **405**, 767–769 (2000).
10. W. Kuch, X. Gao, and J. Kirschner, "Competition between in-plane and out-of-plane magnetization in exchange-coupled magnetic films," Phys. Rev. B **65**, 064406 (2002).
11. H.-Ch. Mertins, F. Schäfers, X. Le Cann, A. Gaupp, and W. Gudat, "Faraday rotation at the 2*p* edges of Fe, Co, and Ni," Phys. Rev. B **61**, R874–R877 (2000).
12. J. B. Kortright, M. Rice, and R. Carr, "Soft-x-ray Faraday rotation at Fe $L_{2,3}$ edges," Phys. Rev. B **51**, 10240–10243 (1995).
13. H.-Ch. Mertins, S. Valencia, D. Abramsohn, A. Gaupp, W. Gudat, and P. M. Oppeneer, "X-ray Kerr rotation and ellipticity spectra at the 2*p* edges of Fe, Co, and Ni," Phys. Rev. B **69**, 064407 (2004).
14. S. Valencia, H.-Ch. Mertins, D. Abramsohn, A. Gaupp, W. Gudat, and P. M. Oppeneer, "Interference effects in the x-ray Kerr rotation spectrum at the Fe 2*p* edge," Physica B **345**, 189–192 (2004).
15. H.-Ch. Mertins, P. M. Oppeneer, J. Kunes, A. Gaupp, D. Abramsohn, and F. Schäfers, "Observation of the x-ray magneto-optical Voigt effect," Phys. Rev. Lett. **87**, 047401 (2001).
16. H.-Ch. Mertins, S. Valencia, A. Gaupp, W. Gudat, P. M. Oppeneer, and C. M. Schneider, "Magneto-optical polarization spectroscopy with soft x-rays," Appl. Phys. A **80**, 1011–1020 (2005).
17. G. A. Prinz, "Magnetoelectronics," Science **282**, 1660–1663 (1998).
18. J. Nouges and I. K. Schuller, "Exchange bias," J. Magn. Magn. Mater. **192**, 203–232 (1999).
19. S. A. Wolf, D. D. Awshalom, R. A. Buhrmann, J. M. Daughton, S. von Molnar, M. L. Roukes, A. Y. Chtchelkanova, and D. M. Treger, "Spintronics: a spin-based electronics vision for the future," Science **294**, 1488–1495 (2001).
20. A. Hubert and R. Schäfer, in *Magnetic Domains*, (Springer Verlag, Berlin, 1998), pp. 24–101.
21. J. Kunes, P. M. Oppeneer, H.-Ch. Mertins, F. Schäfers, A. Gaupp, W. Gudat, and P. Novák, "X-ray Faraday effect at the $L_{2,3}$ edges of Fe, Co, and Ni: theory and experiment," Phys. Rev. B **64**, 174417 (2001).
22. K. Starke, F. Heigl, A. Vollmer, M. Weiss, G. Reichardt, and G. Kaindl, "X-ray magneto-optics in lanthanides," Phys. Rev. Lett. **86**, 3415–3418 (2001).
23. D. S. Kliger, J. W. Lewis, and C. E. Randall, in *Polarized Light in Optics and Spectroscopy*, (Academic, 1990), pp. 231–281.
24. M. Born and E. Wolf, in *Principles of Optics*, (Pergamon, Oxford, 1980) pp. 1–139.
25. H. G. Tompkins and E. A. Irene, in *Handbook of Ellipsometry*, (William Andrew Publishing, Springer, 2005), pp. 237–296.
26. P. M. Oppeneer, in *Handbook of Magnetic Materials*, edited by K. H. J. Buschow, ed., Vol. **13**, (Elsevier, 2001), pp. 229–422.
27. H.-Ch. Mertins, D. Abramsohn, A. Gaupp, F. Schäfers, W. Gudat, O. Zaharko, H. Grimmer, and P. M. Oppeneer, "Resonant magnetic reflection coefficients at the Fe 2*p* edge obtained with linearly and circularly polarized soft X rays," Phys. Rev. B **66**, 184404 (2002).
28. P. M. Oppeneer, H.-Ch. Mertins, D. Abramsohn, A. Gaupp, W. Gudat, J. Kunes, and C. M. Schneider, "Buried antiferromagnetic films investigated by x-ray magneto-optical reflection spectroscopy," Phys. Rev. B **67**, 052401 (2003).
29. W. B. Peatman, in *Gratings, Mirrors, and Slits*, (Gordon and Breach Science Publishers, 1997), pp. 1–54.
30. J. Bardt, W. Frentrup, A. Gaupp, M. Scheer, W. Gudat, G. Ingold, and S. Sasaki, "Elliptically polarizing insertion devices at BESSY II," Nucl. Instrum. Methods Phys. Res. A **467–468**, 21–29 (2001).
31. K. Godehusen, H.-Ch. Mertins, T. Richter, P. Zimmermann, and M. Martins, "Electron-correlation effects in the angular distribution of photoelectrons from Kr investigated by rotating the polarization axis of undulator radiation," Phys. Rev. A **68**, 012711 (2003).
32. M. R. Weiss, R. Follath, K. J. S. Sahwney, F. Senf, J. Bahrdt, W. Frentrup, A. Gaupp, S. Sasaki, M. Scheer, H.-Ch. Mertins, D. Abramsohn, F. Schäfers, W. Kuch, and W. Mahler, "The elliptically polarized undulator beamlines at BESSY II," Nucl. Instrum. Methods Phys. Res. A **467–468**, 449–452 (2001).
33. U. Berges, S. Döring, and C. Westphal, "TGM-Beamline at DELTA," AIP Conf. Proc. **879**, 583–586 (2007).
34. U. Berges, S. Döring, and C. Westphal, "PGM-Beamline at the Undulator U55 at DELTA," AIP Conf. Proc. **879**, 519–522 (2007).
35. A. Gaupp and M. Mast, "First experimental experience with a VUV polarimeter at BESSY," Rev. Sci. Instrum. **60**, 2213–2215 (1989).
36. F. Schäfers, H.-Ch. Mertins, A. Gaupp, W. Gudat, M. Mertin, I. Packe, F. Schmolla, S. di Fonzo, G. Soullié, W. Jark, R. Walker, X. Le Cann, R. Nyholm, and M. Eriksson, "Soft-x-ray polarimeter with multilayer optics: complete analysis of the polarization state of light," Appl. Opt. **38**, 4074–4088 (1999).
37. M. A. MacDonald, F. Schäfers, and A. Gaupp, "A single W/B4C transmission multilayer for polarization analysis of soft x-rays up to 1 keV," Opt. Express **17**, 23290–23298 (2009).
38. E. Arenholz and S. O. Prestemon, "Design and performance of an eight-pole resistive magnet for soft x-ray magnetic dichroism measurements," Rev. Sci. Instrum. **76**, 083908 (2005).
39. N. Jaouen, J.-M. Tonnerre, G. Kapoujian, P. Taunier, J.-P. Roux, D. Raoux, and F. Sirotti, "An apparatus for temperature-dependent soft x-ray resonant magnetic scattering," J. Synchrotron Radiat. **11**, 353–357 (2004).
40. O. Cugat, P. Hansson, and J. M. D. Coey, "Permanent magnet variable flux sources," IEEE Trans. Magn. **30**, 4602–4604 (1994).
41. D. Nolle, M. Weigand, P. Audehm, E. Goering, U. Wiesemann, C. Wolter, E. Nolle, and G. Schütz, "Note: unique characterization possibilities in the ultra high vacuum scanning transmission x-ray microscope (UHV-STXM) "MAXYMUS" using a rotatable permanent magnetic field up to 0.22 T," Rev. Sci. Instrum. **83**, 046112 (2012).
42. J. M. D. Coey, "Permanent magnet applications," J. Magn. Magn. Mater. **248**, 441–456 (2002).

43. R. Bjørk, C. R. H. Bahl, A. Smith, and N. Pryds, "Comparison of adjustable permanent magnetic field sources," J. Magn. Magn. Mater. **322**, 3664–3671 (2010).
44. M. Gilbert, H.-Ch. Mertins, M. Tesch, O. Berges, H. Feilbach, and C. M. Schneider, "TetraMag: a compact magnetizing device based on eight rotating permanent magnets," Rev. Sci. Instrum. **83**, 025109 (2012).
45. H. Höchst, D. Rioux, D. Zhao, and D. L. Huber, "Magnetic linear dichroism effects in reflection spectroscopy: a case study at the Fe $M_{2,3}$ edge," J. Appl. Phys. **81**, 7584–7588 (1997).
46. M. Hecker, P. M. Oppeneer, S. Valencia, H.-Ch. Mertins, and C. M. Schneider, "Soft x-ray magnetic reflection spectroscopy at the 3*p* absorption edges of thin Fe films," J. Electron Spectrosc. Relat. Phenom. **144**, 881–884 (2005).
47. M. C. Biesinger, B. P. Payne, A. P. Grosvenor, L. W. M. Lau, A. R. Gerson, and R. St. C. Smart, "Resolving surface chemical states in XPS analysis of first row transition metals, oxides and hydroxides: Cr, Mn, Fe, Co and Ni," Appl. Surf. Sci. **257**, 2717–2730 (2011).
48. B. V. Crist, in *Handbook of Monochromatic XPS Spectra*, Vol. **2** Commercially Pure Binary Oxides (XPS International Inc., 1999), p. 72.
49. J. Yang, H. Liu, W. N. Martens, and R. L. Frost, "Synthesis and characterization of cobalt hydroxide, cobalt oxyhydroxide, and cobalt oxide nanodiscs," J. Phys. Chem. C **114**, 111–119 (2010).
50. B. L. Henke, E. M. Gullikson, and J. C. Davis, "X-ray interactions: photoabsorption, scattering, transmission, and reflection at E=50-30000 eV, Z=1-92," At. Data Nucl. Data Tables **54**, 181–342 (1993), http://henke.lbl.gov/optical_constants/.
51. F. Schäfers and M. Krumrey, "REFLEC—a program to calculate soft x-ray optical elements and synchrotron radiation beamlines," Tech. Rep. BESSY TB 201, Berlin (1996).
52. W. L. Roth, "Magnetic structures of MnO, FeO, CoO, and NiO," Phys. Rev. **110**, 1333–1341 (1958).
53. W. L. Roth, "The magnetic structure of Co_3O_4," J. Phys. Chem. Solids **25**, 1–10 (1964).
54. B. Sonntag, R. Haensel, and C. Kunz, "Optical absorption measurements of the transition metals Ti, V, Cr, Mn, Fe, Co, Ni in the region of 3*p* electron transitions," Solid State Commun. **7**, 597–599 (1969).
55. M. Fanfoni, S. Modesi, N. Motta, M. de Crescenzi, and R. Rosei, "Comparison between extended x-ray-absorption and extended electron energy-loss fine-structure results above the $M_{2,3}$ edge of cobalt," Phys. Rev. B **32**, 7826–7829 (1985).
56. Z.-X. Shen, J. W. Allen, P. A. P. Lindberg, D. S. Dessau, B. O. Wells, A. Borg, W. Ellis, J. S. Kang, S.-J. Oh, I. Lindau, and W. E. Spicer, "Photoemission study of CoO," Phys. Rev. B **42**, 1817–1828 (1990).
57. M. A. Langell, M. D. Anderson, G. A. Carson, L. Peng, and S. Smith, "Valence-band electronic structure of Co_3O_4 epitaxy on CoO(100)," Phys. Rev. B **59**, 4791–4798 (1999).
58. P. Steiner, R. Zimmermann, F. Reinert, T. Engel, and S. Hüfner, "3*s*- and 3*p*-core level excitations in 3*d*-transition metal oxides from electron-energy-loss spectroscopy," Z. Phys. B **99**, 479–490 (1996).
59. J. M. McKay, M. H. Mohamed, and V. E. Heinrich, "Localized 3*p* excitations in 3*d* transition- metal-series spectroscopy," Phys. Rev. B **35**, 4304–4309 (1987).
60. C. A. Strydom and H. J. Strydom, "X-ray photoelectron spectroscopy studies of some cobalt(II) nitrate complexes," Inorganica Chimica Acta **159**, 191–195 (1989).
61. M. Takahashi and J.-I. Igarashi, "Local approach to electronic excitations in MnO, FeO, CoO, and NiO," Phys. Rev. B **54**, 13566–13574 (1996).
62. X-ray data booklet, Center for X-ray Optics and Advanced Light Source Lawrence Berkeley National Laboratory, 1–3, http://xdb.lbl.gov/.
63. ReMagX, computer code available at: http://www.remagx.org.
64. H. Höchst, D. Zhao, and D. L. Huber, "Strong angular effects in reflection MCD measurements of $M_{2,3}$ transitions utilizing a newly developed quadruple reflection polarizer," J. Electron Spectrosc. Relat. Phenom. **80**, 469–472 (1996).
65. H. Höchst, D. Rioux, D. Zhao, and D. L. Huber, "Directional magnetization effects in magnetic circular dichroism spectra of Fe," Phys. Rev. B **65**, 064439 (2002).
66. S. Valencia, A. Kleibert, A. Gaupp, J. Rusz, D. Legut, J. Bansmann, W. Gudat, and P. M. Oppeneer, "Quadratic x-ray magneto-optical effect upon reflection in a near- normal-incidence configuration at the *M* edges of 3*d*-transition metals," Phys. Rev. Lett. **104**, 187401 (2010).
67. M. A. Schröder, "Magnetooptische Kerr-Effekte im VUV an Eisen und Eisensystemen," DESY report: DESY-THESIS-2000-050, (2000).
68. J. M. Ballantyne, "Kerr magneto-optic effect in thin cobalt films," J. Opt. Soc. Am. **54**, 1352 (1964).
69. S. Uba, L. Uba, A. Y. Perlov, A. N. Yaresko, V. N. Antonov, and R. Gontarz, "Experimental and *ab initio* theoretical study of optical and magneto-optical properties of Co/Cu multilayers," J. Phys. **9**, 447–460 (1997).
70. S. Uba, L. Uba, and R. Gontarz, "Magnetooptical Kerr spectroscopy of Co/Pd layered structures," IEEE Trans. Magn. **30**, 806–808 (1994).
71. S. Valencia, A. Gaupp, W. Gudat, H.-Ch. Mertins, P. M. Oppeneer, D. Abramsohn, and C. M. Schneider, "Faraday rotation spectra at shallow core levels: 3*p* edges of Fe, Co, and Ni," New J. Phys. **8**, 254 (2006).
72. M. J. Freiser, "A survey of magnetooptic effects," IEEE Trans. Magn. **4**, 152–161 (1968).
73. J. Geissler, E. Goering, M. Justen, F. Weigand, G. Schütz, J. Langer, D. Schmitz, H. Maletta, and R. Mattheis, "Pt magnetization profile in a Pt/Co bilayer studied by resonant magnetic x-ray reflectometry," Phys. Rev. B **65**, 020405(R) (2001).
74. J. B. Kortright and A. Fischer-Colbrie, "Standing wave enhanced scattering in multilayer structures," J. Appl. Phys. **61**, 1130–1333 (1987).